ADVANCED MATERIALS

Supporting Information

for *Adv. Mater.,* DOI: 10.1002/adma.202102113

Magnetic Dynamic Polymers for Modular Assembling and Reconfigurable Morphing Architectures

Xiao Kuang, Shuai Wu, Qiji Ze, Liang Yue, Yi Jin, S. Macrae Montgomery, Fengyuan Yang, H. Jerry Qi, and Ruike Zhao**

Supporting Information

Magnetic Dynamic Polymers for Modular Assembling and Reconfigurable Morphing Architectures

Xiao Kuang, Shuai Wu, Qiji Ze, Liang Yue, Yi Jin, S. Macrae Montgomery, Fengyuan Yang, H. Jerry Qi, Ruike Zhao**

Table of content

Supplementary Methods

Gel permeation chromatography (GPC). GPC analysis of linear prepolymers was conducted using a GPC (Agilent, Santa Clara, CA, USA). The prepolymer concentration was 5 mg mL^{-1}. $CHCl_3$ was used as eluent with a flow rate of 0.45 mL min^{-1}, and the system was calibrated using $CHCl_3$ with polystyrene standard samples (American Polymer Standards Corporation, Mentor, OH, USA).

Nuclear magnetic resonance (NMR). Proton nuclear magnetic resonance (^{1}H-NMR) spectrum of prepolymer was acquired on a Bruker AVANCE III HD 500 (Billerica, MA, USA). Chemical shifts were reported in ppm relative to signals from the NMR solvent of $CDCl_3$ (7.26 ppm for ^{1}H spectrum).

Scanning electron microscopy (SEM). SEM images were acquired on a Hitachi SU8010 SEM (Hitachi Ltd, Chiyoda, Tokyo, Japan) using an acceleration voltage of 5 kV. The unmagnetized NdFeB microparticles were dispersed in alcohol and then cast on a copper tape. After evaporation of the solvent, the particles on the tape were gently pressed for a reliable attachment. The cryo-fractured magnetic dynamic polymer (MDP) sample was obtained by breaking in liquid nitrogen and the crack surface was exposed for observation. Before the test, samples were treated with a thin layer of gold for 45 s by a Quorum Q 150T sputter coater (Quorum Tech. Ltd, Lewes, UK).

Fourier transform infrared spectra (FTIR). FTIR spectra were recorded by a Nicolet iS50 FTIR spectrometer (Thermo Scientific, Waltham, MA, USA). The liquid prepolymer and solid cross-linked polymer were characterized by attenuated total reflectance (ATR) mode. The spectra were obtained from 650 to 4000 cm^{-1} with a resolution of 2 cm^{-1} by averaging 32 scans.

Creep tests. The creep tests were conducted on a DMA (Q800, TA Instruments, New Castle, DE, USA) in a tension mode. The sample was equilibrated at a predetermined

temperature for 10 min, then a constant stress was applied, and the strain was monitored as a function of time. Creep tests were performed under the conditions of various temperatures and applied stress. To measure the zero-shear viscosity of MDP, a slow strain rate (< 0.005 min^{-1}) was applied by using lower stresses at higher temperatures.

Thermogravimetric Analysis (TGA). TGA was performed on an STA 6000 Simultaneous Thermal Analyzer (PerkinElmer, Waltham, MA ,USA). About 8 - 10 mg of samples were loaded in a ceramic pan. The tests were performed under a constant stream of nitrogen gas with a flow rate of 20 mL min^{-1}. The temperature ramped from 50 - 700 ºC at a heating rate of 10 °C min^{-1}.

Magnetic properties. The magnetic properties of MDP were measured using a Vibrating Sample Magnetometer (VSM, 7400A series, Lake Shore Cryotronics, Inc., Chicago, IL, USA). The magnetic moments of a composite sample (4 × 4 × 1 mm) were recorded under the magnetic field *B* scanned from -1.5 T to 1.5 T. The corresponding magnetic moment densities were calculated by dividing the magnetic moments with the sample volume. The remanent magnetization (M_r) of the directly magnetized samples was measured as 75 kA m^{-1}.

Modular assembling and welding experiment. For uniform modular assembling, a rectangular strip (dimension: 36 × 6 × 0.9 mm) was cut by a blade and then assembled by the dipole attraction. The assembly was treated under an Infrared (IR) heating lamp (250 W, 120 V, SATCO, NY, USA) for 5 min with the surface temperature at around 80 ºC. The uniaxial tension test was used to quantitatively evaluate the welding efficiency. The rectangular strips (dimension: 25 × 4 × 0.9 mm) with magnetization along the longitudinal direction were first cut by a sharp blade and then put together by gentle force. Afterward, the assembled samples were treated at different conditions and further

stored at room temperature for one day before the test. The ratio of material fracture strain between the welded sample and original bulk material was calculated as welding efficiency. For 2D structural assembling, square MDP modules (dimension: 6 × 6 × 0.9 mm) with two different magnetization patterns: a single-directional magnetization and a bidirectional magnetization, were prepared. Different 2D structures were assembled using different combinations of modules and logics. The assemblies were then sandwiched between PTFE films with gentle pressure and treated in an oven at 80 ºC for 20 min, resulting in the seamless welding of the modules. For the magnetic-driven remote navigation and assembling demonstrations, structures are assembled using remotely applied rotating magnetic fields (3 mT, 1 Hz) and welded by remotely applied laser (1W, Sanwu, Jiangsu, China).

Magnetization reprogramming experiment. In-situ magnetization reprogramming was observed using a digital microscope (Celestron, Torrance, CA, USA) coupled with a pair of electromagnetic coils. A thin layer of an MDP sample sandwiched between glasses was heated up to 110-120 ºC using a heat gun, and then a uniform magnetic field of 35 mT was applied to realign the particles. Ex-situ observation of cyclic magnetization realignment was conducted by treating the sample inside a Halbach array magnet (the central magnetic field of 35 mT) under IR illumination at 110 ºC for 2 min. A square shape array containing a 4 × 4 MDP cells (9 × 9 × 1 mm) was manufactured by encapsulating MDP cells in a silicone substrate (Ecoflex 00-50, Smooth-on, Inc., Macungie, PA, USA.) with a hinge design. The MDP resin was in-situ cured at ~50ºC

in the 4 × 4 array of grooves in silicone mold followed by coating a thin layer of silicone for encapsulation. The array was firstly magnetized in a folding shape. To selectively reprogram the magnetization, aluminum foil photomasks were used to selectively expose the cells to IR light with the heating temperature at 110 - 120 ºC. Meanwhile, a magnetic field provided by the Halbach array magnet realigned the magnetization with a duration of 2-3 min. After extinguishing the IR light, the sample was kept in the magnetic field for 5 min to cool down and then annealed in an oven at 60 ºC for 10 min. To reprogram the magnetization with complex patterns, both the photomasks and magnetic field were altered multiple times until the whole reprogramming was finished.

3D architectures reshaping and mechanical characterization. The 2D kirigami structures with helical cuts and concentric arc cuts were fabricated by curing the MDP resin in silicone molds (Ecoflex 00-50, Smooth-on, Inc., Macungie, PA, USA). After demolding, the structures were glued on a square plastic plate with a circular hole. The structures were magnetized in mechanically stretched-out configurations. Remote reforming of architecture was conducted by putting a cylinder magnet (D50 × 20 mm, NdFeB N52-Grade, AOMAG, Fuzhou, Fujian, China) below the sample with a distance of 35 or 25 mm and exposing the MDP architecture to IR illumination for around 15 or 30 min for the helical and the concentric arc kirigami structures, respectively. The temperature was set at around 80 ºC for the top surface. After the treatment, the stress-free architectures were obtained and kept at room temperature before testing. The original and the reshaped architectures were mounted on a plastic stage for magnetic

actuation tests under a uniform external magnetic field. The mechanical tests of original and reshaped architectures were measured by Instron 3340 (Instron, Norwood, MA, USA) using a load cell of 100 N at room temperature with a loading speed of 40 mm min^{-1}. A printed plastic stick with a tiny hole on the bottom was connected to the center of the architectures by a soft thread to enable effective force transmission between the sample and load cell without constraining rotation.

Finite-element analysis of the reshaped 3D kirigami. Finite element analysis was implemented through the commercial software ABAQUS 2018 (Dassault Systèmes, France) to simulate the shape morphing process of the reshaped kirigami architectures. 2D structures were modeled with designed dimensions (Figure S19a and Figure S20a) using C3D8RH element. The neo-Hookean constitutive model was adopted with Young's modulus of 400 kPa and bulk modulus of 400 MPa. First, out-of-plane displacements were applied to the 2D models to match the reshaped 3D architectures in the experiments. Then, stress-free configurations were exported for simulations of mechanical actuations.

Dynamic polymer network relaxation analysis

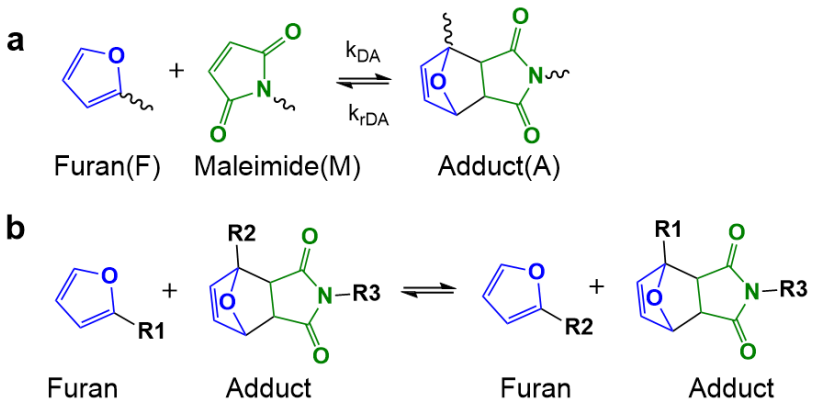

Scheme S1. a) Scheme of thermally reversible Diels-Alder (DA) reaction between reactants of furan /maleimide and product of adduct. The forward DA reaction rate constant is k_{DA} and the retro DA reaction rate constant is k_{rDA}. b). Bond exchange reaction between furan and adduct.

For the thermally reversible Diels-Alder (DA) reaction between furan and maleimide, the forward DA reaction (rate constant k_{DA}) is favored forming adduct at low temperatures; retro DA reaction (rDA) is dominant by cleaving the adduct (rate constant k_{rDA}) at elevated temperatures. In DA based dynamic polymer (DP), both reaction kinetics and thermodynamics are influenced by temperature. A scaling relationship between the dynamic bond lifetime and relaxation time of DA polymer has been previously established [1]. This kind of transient network achieves relaxation in the form of clusters with characteristic percolation cutoff size [2]. A scaling relationship between bond lifetime and relaxation time was derived based on Semenov−Rubinstein theory [3-4]. The maximum relaxation time of the dynamic network τ_{DP} corresponds to the rheological lifetime of the cluster, which is proportional to the bond lifetime τ_b and the relative distance to the gel point ε:

$$\tau_{DP} \cong \tau_b \varepsilon \,, \varepsilon = \frac{p - p_{gel}}{p_{gel}} \tag{S1}$$

where τ_b is the lifetime of dynamic linkage ($\tau_b = 1/k_{rDA}$); p is the conversion of the limiting reagent (maleimide) or the percentage of dynamic linkages; p_{gel} is the gel-point

conversion of DP between bismaleimide and furan grafted prepolymer. The p_{gel} can be predicted by the Flory-Stockmayer equation [5]:

$$p_{gel} = \frac{1}{\sqrt{r(f_1 - 1)(f_2 - 1)}} \quad (S2)$$

The functionality of synthesized furan grafted prepolymer, $f_1 = 13$, and functionality of bismaleimide cross-linker, $f_2 = 2$. For DP and MDP with maleimide/furan ratio $r = 0.15$, p_{gel} is calculated to be 0.74, indicating the network and fluid transition near a dynamic linkage conversion of 74 %.

The effect of temperature on chemical reaction rate constant (k) follows the Arrhenius' law:

$$k = k_0 \exp(-\frac{E_{a,r}}{RT}) \quad (S3)$$

where k_0 is the reference reaction rate constant at infinite temperature; $E_{a,r}$ is the activation energy of rDA reaction; R is the gas constant, and T is the absolute temperature. Therefore, we can have a temperature-dependent dynamic bond lifetime:

$$\tau_b = \tau_{b,0} \exp(\frac{E_{a,r}}{RT}) \quad (S4)$$

By combining equation (1) and (4), we can express the network relaxation time as:

$$\tau_{DP} \cong \tau_b \varepsilon = \tau_{b,0} \exp(\frac{E_{a,r}}{RT})(\frac{p - p_{gel}}{p_{gel}}) \quad (S5)$$

τ_{DP} can be directly measured by stress relaxation using DMA or rheology test. p can be measured by DSC or FTIR. p_{gel} is predicted by Flory-Stockmayers equations. It is noted that the equation is valid for $p > p_{gel}$, when the material is still a cross-linked network.

As above-mentioned, the DA reaction thermodynamics is also influenced by temperature. The temperature variant equilibrium conversion (p_{eq}) is determined by the reaction equilibrium constant (K_{eq}) by the following equation:

$$K_{eq} = \frac{k_{rDA}}{k_{DA}} = \frac{[A]}{[F][M]} = \frac{1}{[M]_0} \frac{p_{eq}}{(1 - p_{eq})(r^{-1} - p_{eq})} \quad (S6)$$

where [A], [F], [M] are the concentrations of adduct, furan, and maleimide groups, respectively; $[M]_0$ is the molar concentration of the initial maleimide functional group. According to Van't Hoff equations, the effect of temperature on reaction equilibrium

constant is expressed by:

$$\ln K_{eq} = -\frac{\Delta H_r^{\ 0}}{RT} + \frac{\Delta S_r^{\ 0}}{R} \tag{S7}$$

where ΔH_r^0 is the enthalpy of reaction, and ΔS_r^0 is the entropy of DA reaction. As K_{eq} and p_{eq} decrease with temperature, p_{eq} can be lower than p_{gel} above a critical temperature (T_{gel}). Consequently, the cross-linked polymer network transforms into mobile viscous clusters at elevated temperatures.

Supplementary figures: Figures S1-S24

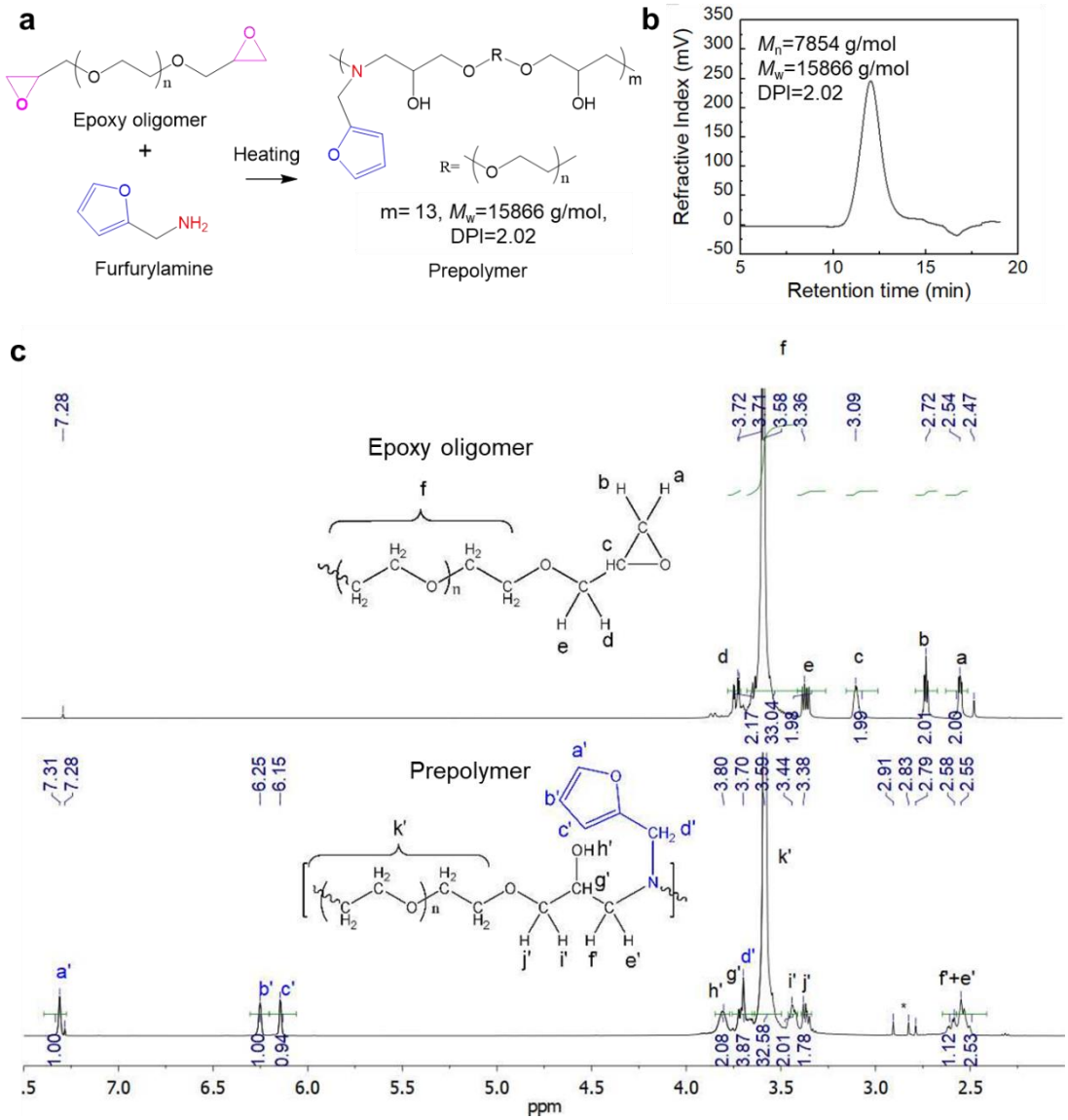

Figure S1. Synthesis and characterization of furan grafted prepolymer. a) Synthesis of furan grafted prepolymer by the reaction between epoxy oligomer and furfurylamine by ring-opening reaction at elevated temperatures in DMF. b) GPC profile of the linear prepolymer in the chloroform ($CHCl_3$) mobile phase. c) ^1H NMR spectrum of epoxy oligomer and furan grafted prepolymer in $CDCl_3$.

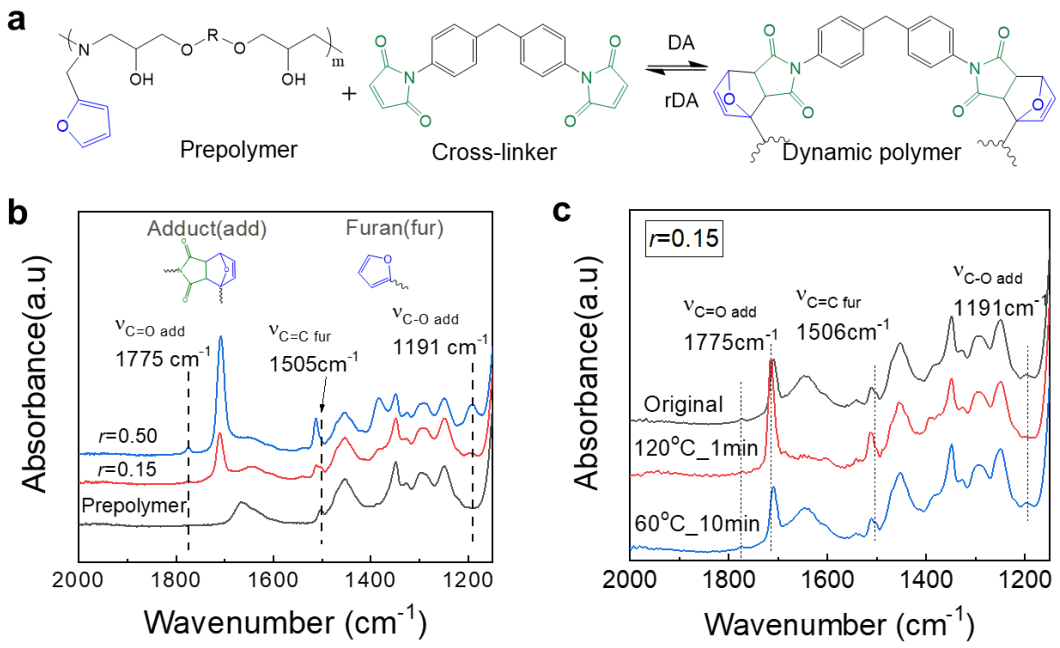

Figure S2. Synthesis and chemical structural characterization of DP. a) Schematics reaction between furan grafted prepolymer and bismaleimide cross-linker by Diels-Alder reaction (DA) and retro Diels-Alder reaction (rDA). b) FTIR spectrum of prepolymer and DP with different maleimide/furan ratios (*r*) within the wavenumber of 1150 - 2000 cm^{-1}. C=O stretching vibration at 1775 cm^{-1}, C-O stretching vibration at 1191 cm^{-1} are the characteristic peaks of DA adduct. C=C stretching vibration at 1505 cm^{-1} is a characteristic peak of the furan group. c) FTIR of DP (r = 0.15) in the heating-cooling cycle. Cross-linked DP was heated to 120 ºC to break the cross-linking and then annealed at 60 ºC for 10 min to reform the dynamic linkages.

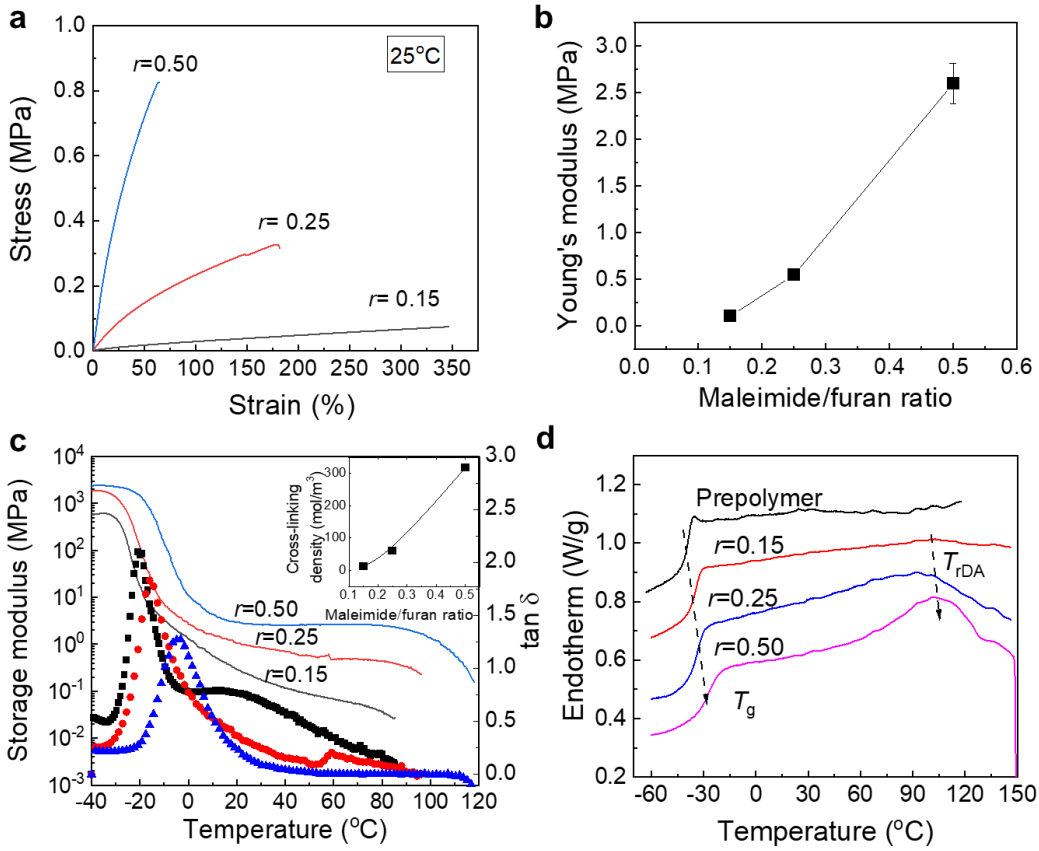

Figure S3. Mechanical and thermomechanical characterization of DP. a) Tensile stress-strain curves of DP with various *r* values. b) Young's modulus as a function of maleimide/furan ratios. c) DMA heating curves of DP with different *r* values and cross-linking densities (μ) evaluated by the rubbery modulus (E_r) at 60 °C by $\mu = E_r/(3RT)$. d) DSC heating curves of DP with different *r* values. Glass transition temperature (T_g) and rDA temperature (T_{rDA}) were determined from the curves.

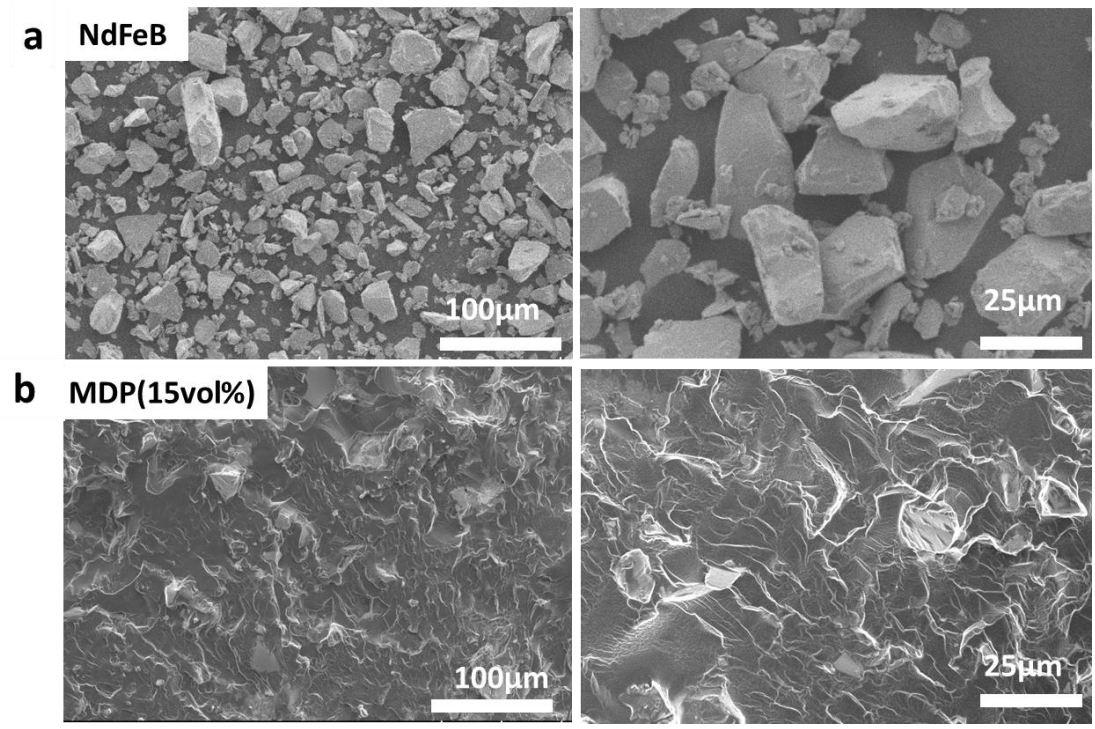

Figure S4. SEM images of NdFeB microparticles with an average size of 25μm (a) and the MDP containing 15 vol % of 25μm NdFeB particles (b).

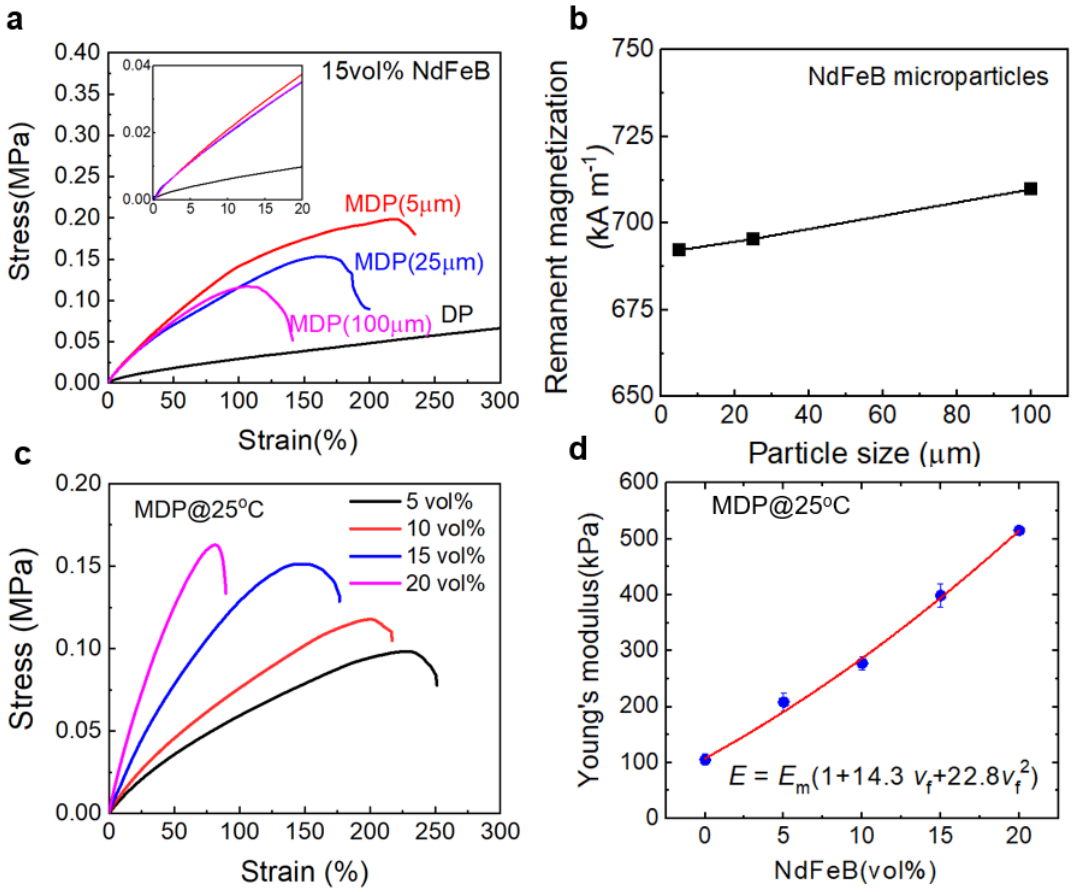

Figure S5. Physical properties of MDPs. a) Comparison of tensile stress-strain curves of DP and MDPs containing 15 vol% of NdFeB microparticles with three different particle sizes. b) The remanent magnetization of NdFeB particles as a function of particle size. [8]. c) Tensile stress-strain curves of MDPs with different loadings of NdFeB microparticle (25 μm). d) Young's moduli of the MDPs as a function of NdFeB microparticle (25 μm) volume concentrations from 0 to 20 vol%. The curves are fitted by the Guth-Gold model with modified parameters [9].

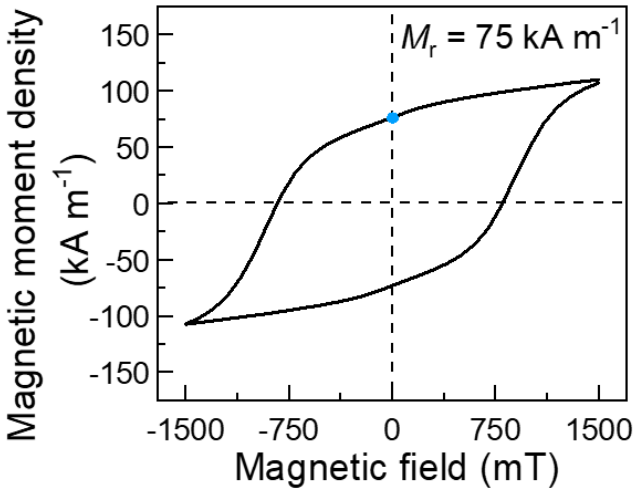

Figure S6. Magnetization hysteresis loop of the MDP with 15 vol% of NdFeB microparticles. The remanent magnetization (M_r) of directly magnetized samples was measured as 75 kA m^{-1}.

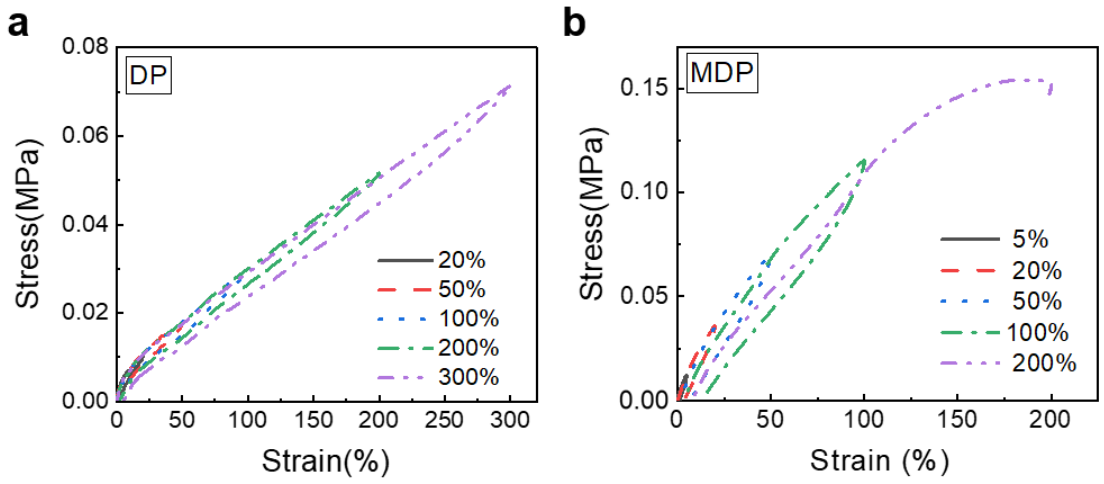

Figure S7. Cyclic loading-unloading stress-strain curves of the DP (a) and the MDP containing 15vol% of 25 μm NdFeB (b). The strain rate is 0.3 min^{-1}.

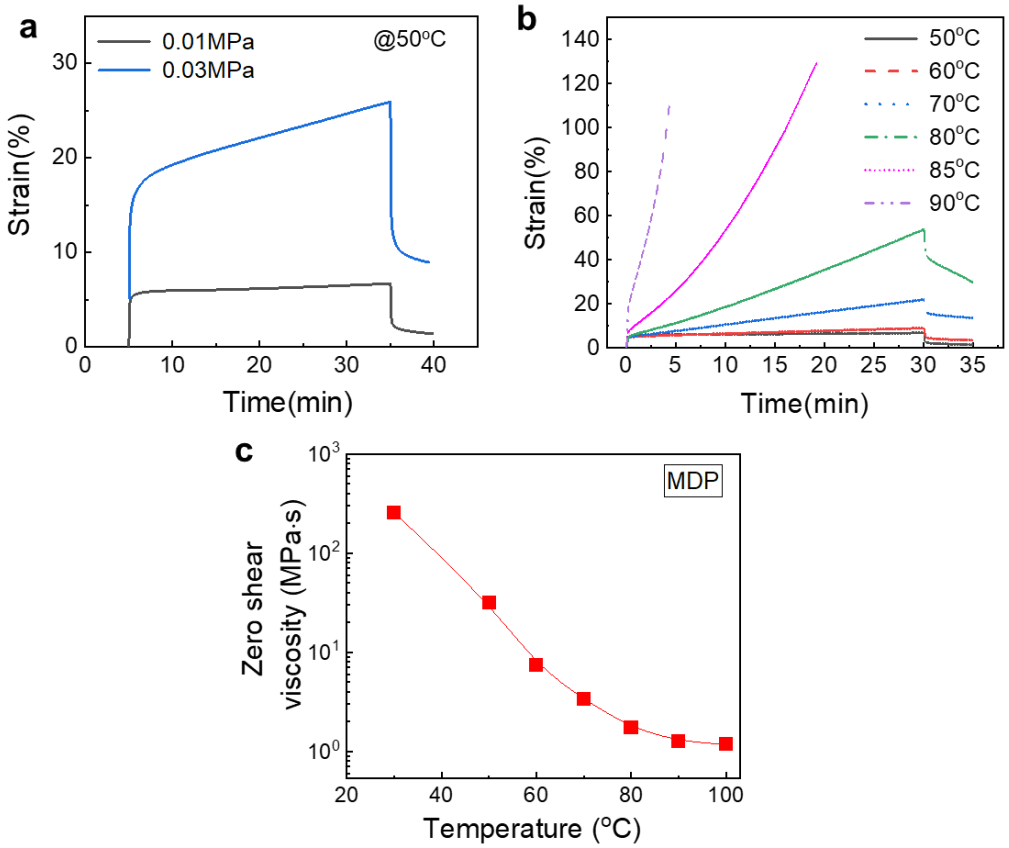

Figure S8. Creep tests of the MDP. a) Creep test curves of the MDP under different applied stress at 50 °C. b) Creep strain as a function of time of the MDP at different temperatures with constant applied stress of 0.01 MPa. c) Zero-shear viscosity as a function of temperature for the MDP. Zero-shear viscosity was calculated by the ratio of the applied stress and a low strain rate at the steady flow region on creep curves.

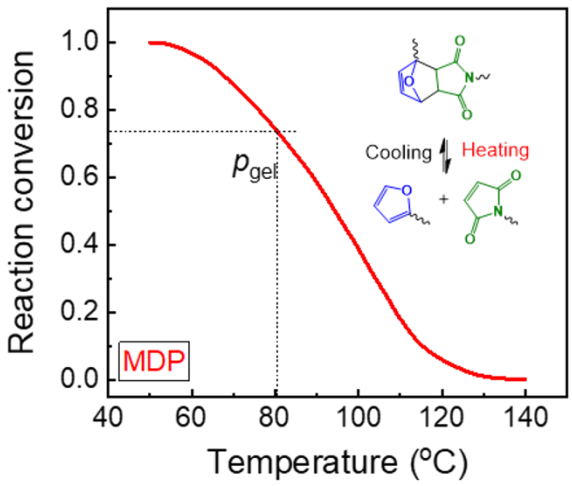

Figure S9. Percentage of dynamic linkages in the MDP as a function of temperature derived from the area integration under the endothermal peak on DSC heating curve in Figure 2d. Inserted is the scheme of DA and rDA reaction upon cooling and heating, respectively. The polymer network transforms into mobile clusters with reaction conversion below p_{gel} and depolymerizes into small segments for further heating. The temperature is marked based on the predicted gel point conversion of 74%.

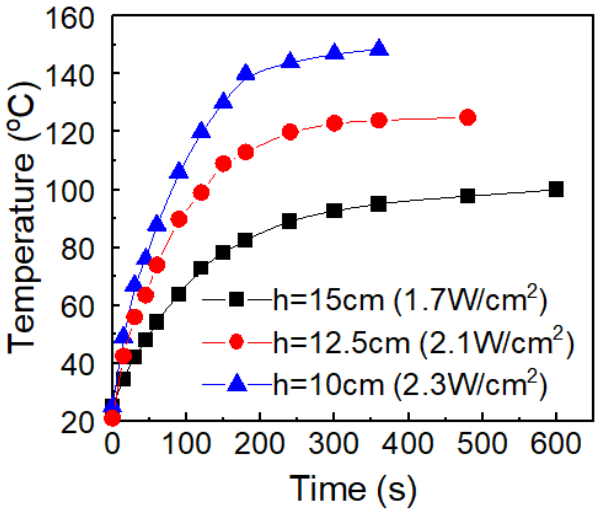

Figure S10. Heating temperature as a function of the IR illumination time with different distances between the IR bulb and the MDP sample during photothermal heating. The surface temperature is measured by a thermal imaging camera. The light intensity was measured by a Laser Power Meter (Molectron PM500, Molectron Detector Inc., Portland, Oregon, USA).

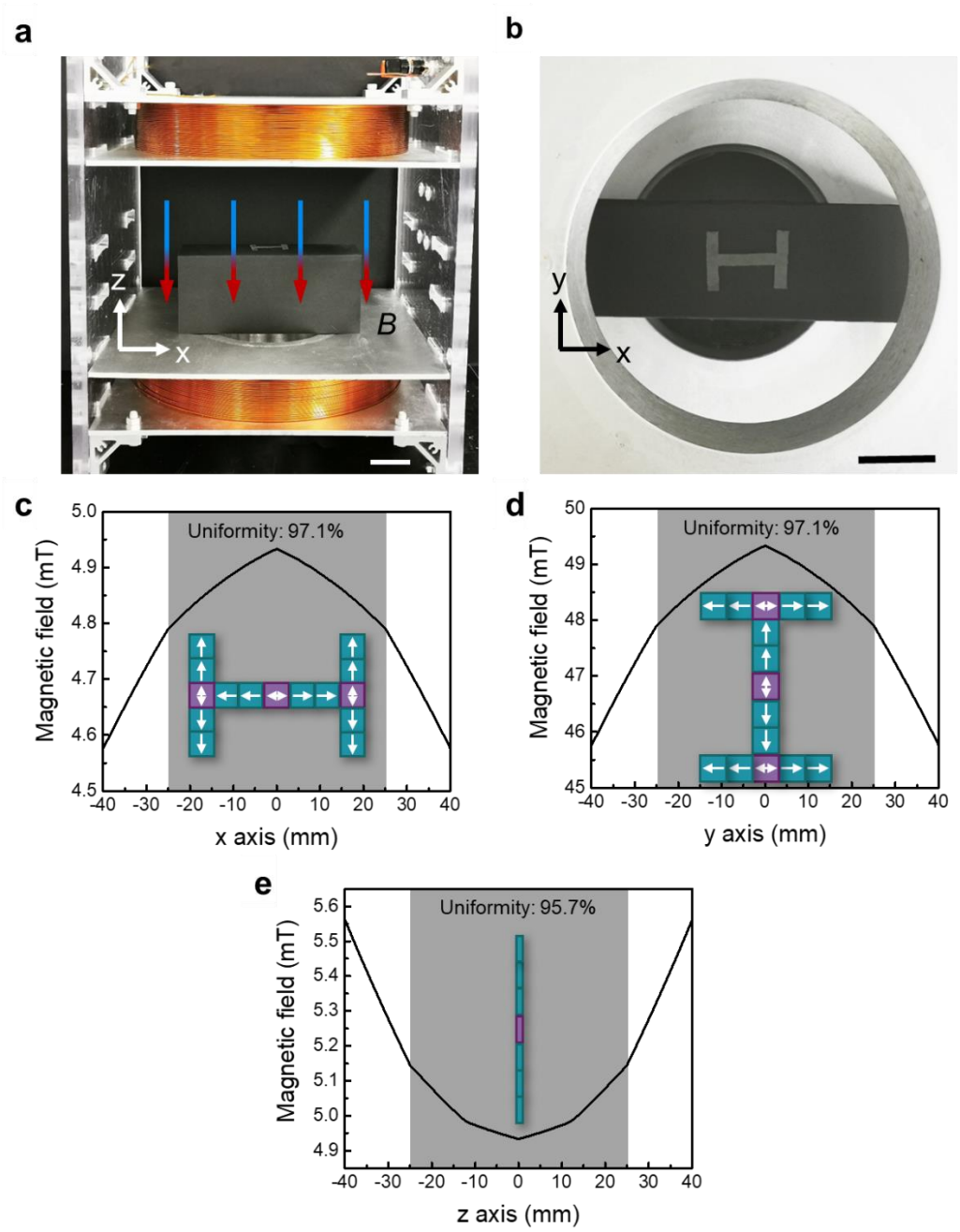

Figure S11. The electromagnetic coils with a spacing of 200 mm for magnetic actuation. The side view (a) and top view (b) of the setup. Magnetic field distribution along *x*-axis (c), *y*-axis (d), and *z*-axis (e) with the currents of 1A in the coils. A schematic of the H-shape assembly in Figure 3 was included to show the relative dimension. Scale bars, 4 cm.

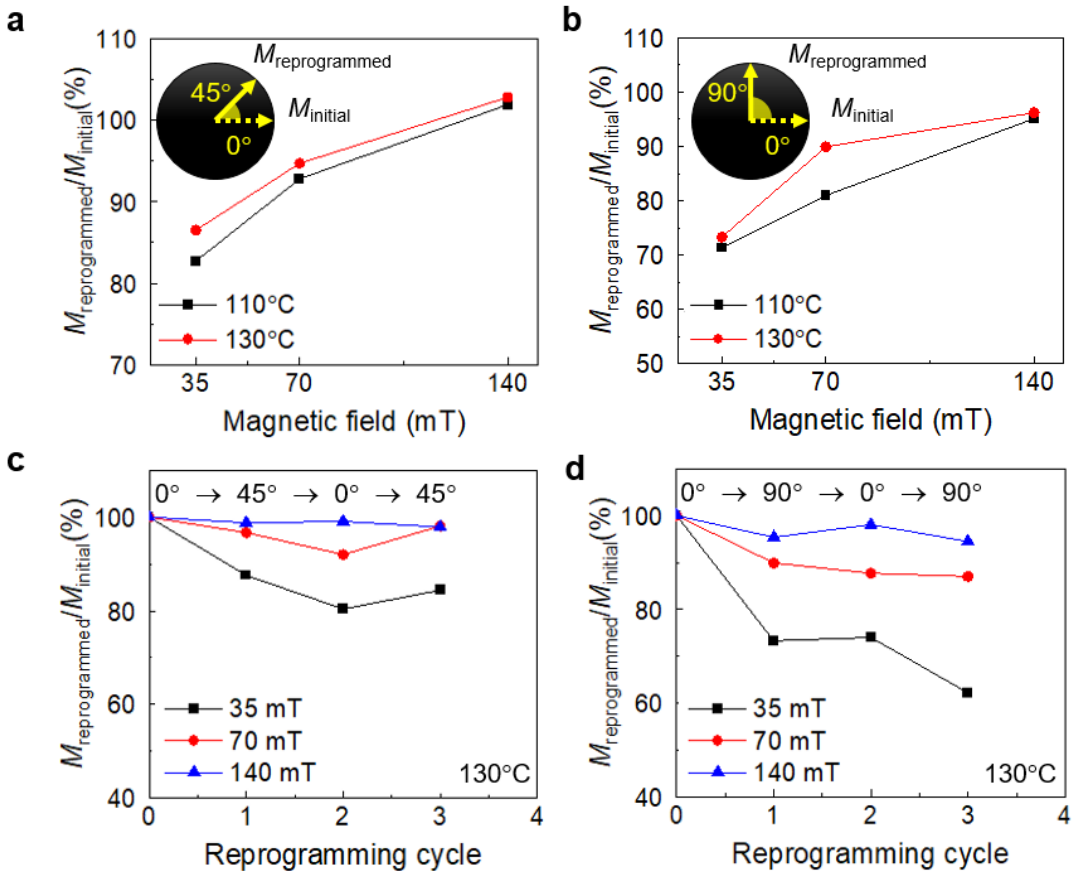

Figure S12. Reprogramming efficiency of MDP with 15 vol% NdFeB with respect to the applied magnetic field and temperature for a) reprogramming with 45° reprogrammed direction, b) reprogramming with 90° reprogrammed direction, c) reprogramming between 0° and 45° directions for three successive cycles, and d) reprogramming between 0° and 90° directions for three successive cycles. The reprogramming process was conducted by applying a predetermined magnetic field (35 mT, 70 mT, or 140 mT) with a realignment angle (45° or 90° to the initial magnetization direction) at an elevated temperature (110 °C or 130 °C) for 5 min. The reprogramming efficiency is calculated by the ratio of reprogrammed magnetization to the initial magnetization.

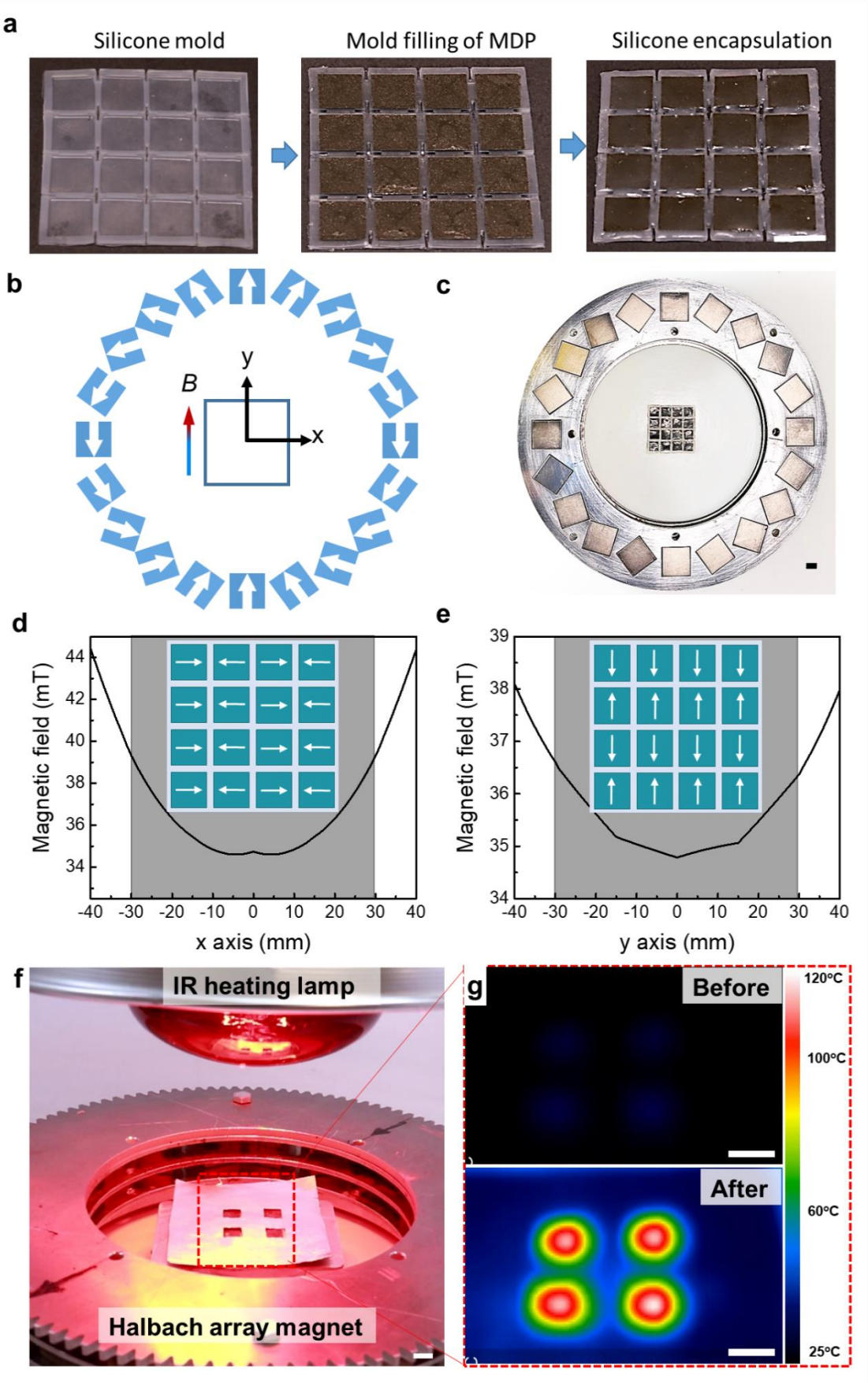
a
Silicone mold
Mold filling of MDP
Silicone encapsulation
b
B
y
x
c
d
Magnetic field (mT)
x axis (mm)
e
Magnetic field (mT)
y axis (mm)
f
IR heating lamp
Halbach array magnet
g
Before
After
120°C
100°C
60°C
25°C

Figure S13. Design and in-situ magnetization reprogramming of a 4 × 4 MDP array. a) Fabrication procedure of the silicone rubber encapsulated MDP array. The schematics (b) and picture (c) of the Halbach array. Magnetic field distribution along the *x*-axis (d) and *y*-axis (e) of the Halbach array. A schematic of the MDP array from (a) is included to show the relative dimension. f) Setup for in-situ magnetization reprogramming: the Halbach array magnet (central uniform magnetic field of 35 mT), an IR light bulb as a light source, and an aluminum foil with patterned holes as a photomask. g) Temperature profile of the 4 × 4 MDP array before and after IR illumination when using the aluminum photomask to selectively expose four discrete cells. Local temperature goes up to 110-120 ^{o}C in 2 min. During magnetization reprogramming, the high temperature is maintained for around 2 min before cooling down in the magnetic field. After that, the sample is taken out and treated in an oven at 60 ^{o}C for 10 min to ensure good cross-linking in each reprogramming step. Scale bars for all images, 10 mm.

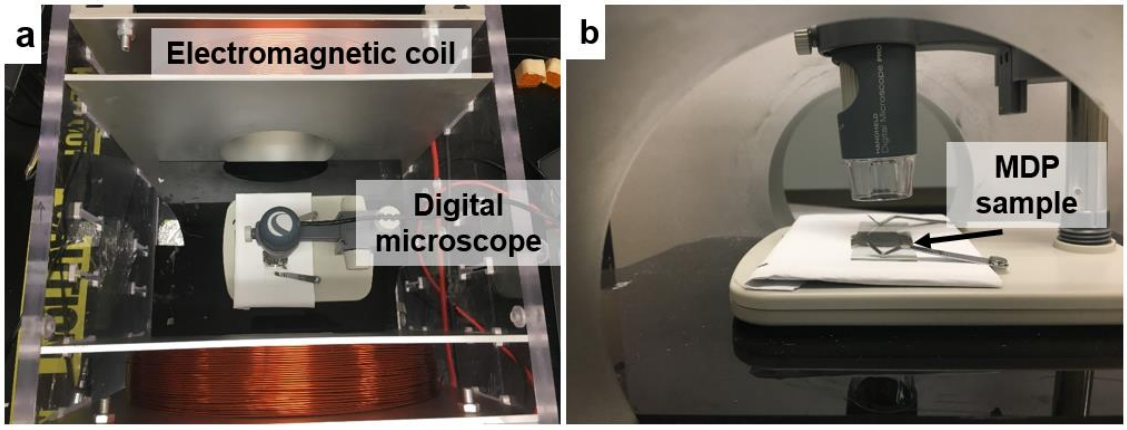

Figure S14. Setup of a digital microscope coupled with a pair of electromagnetic coils for in-situ observation of dipole rotation. The MDP sample is sandwiched between two glass slides and heated to 110-120 ºC using a heat gun. A uniform magnetic field of 35 mT is applied to realign the magnetic particles.

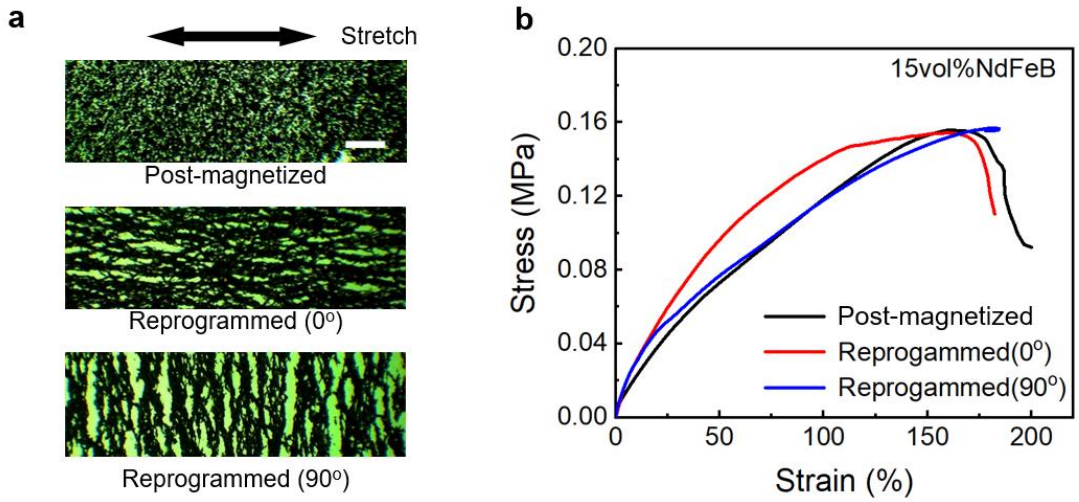

Figure S15. Microscopic morphology and mechanical characterization of post-magnetized and reprogrammed MDP samples. a) Optical microscopic images of post-magnetized and reprogrammed MDP samples with different orientations to the stretching direction of the tensile test. Scale bar, 200 μm. b) Tensile stress-strain curves of the post-magnetized and reprogrammed MDP samples with 0° and 90° alignment to stretching direction.

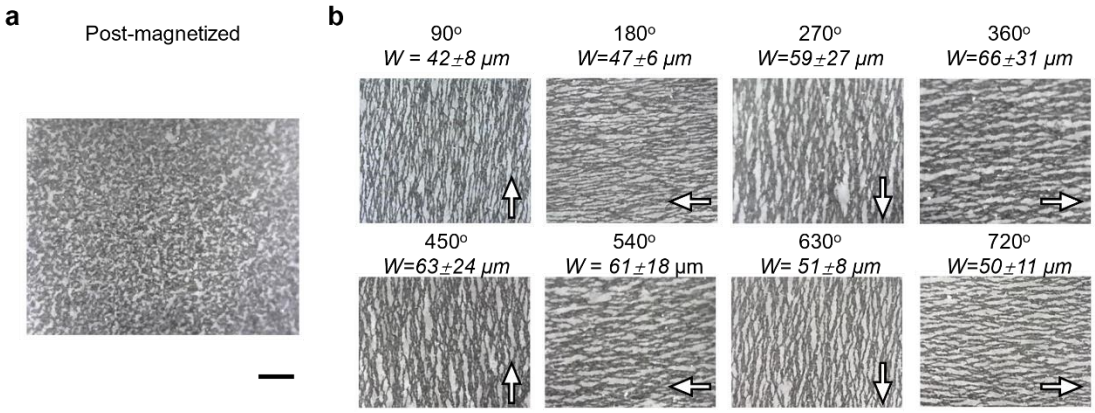

Figure S16. a) Optical microscopy image of MDP before reprogramming. b) Optical microscopy images of MDP after multiple cycles of reprogramming with 720° chain rotation. *W* is the average width of alignment regions. The average and standard deviation values are based on the measurements of 30 chains in each image. Scale bar: 500 μm.

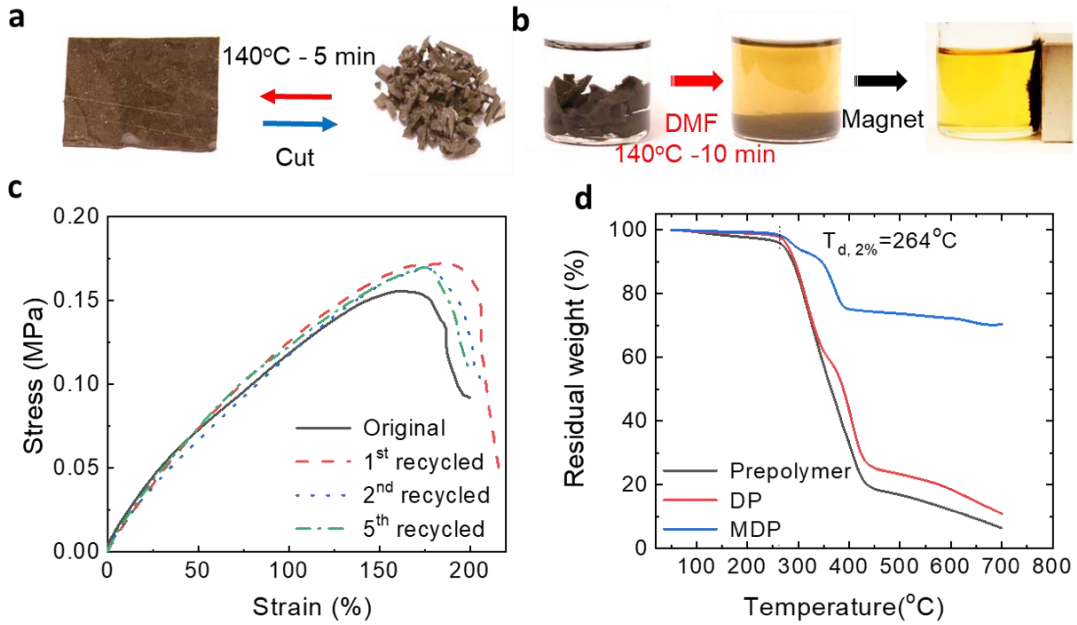

Figure S17. Thermal recycling of the MDP. a) Picture of reprocessing/recycling the MDP by hot compression at 140 ºC for 5 min. b) The MDP is completely dissolved in DMF at 140 ºC for 10 min. The magnetic microparticles are separated from the solution by a magnet. c) Tensile stress-strain curves of original and hot recycled the MDP. Recycled materials have nearly the same mechanical properties for at least five recycling cycles. c) TGA heating curves of the prepolymer, DP, and MDP, showing good thermal stability with 2 wt% weight loss temperature at 264 ºC.

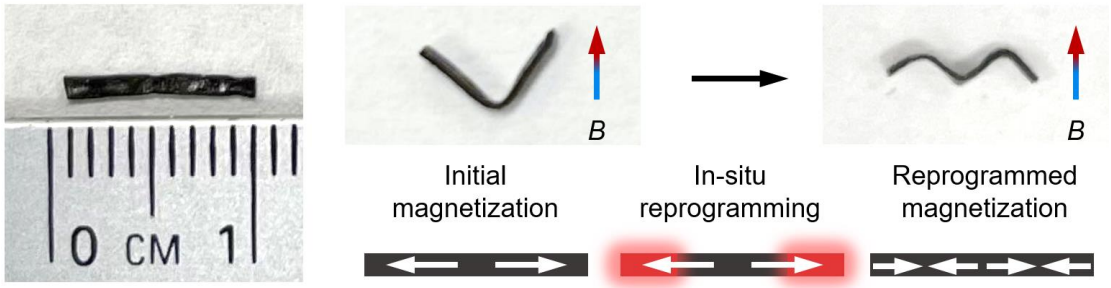

Figure S18. In-situ magnetization reprogramming of MDP with the millimeter-scale reprogramming.

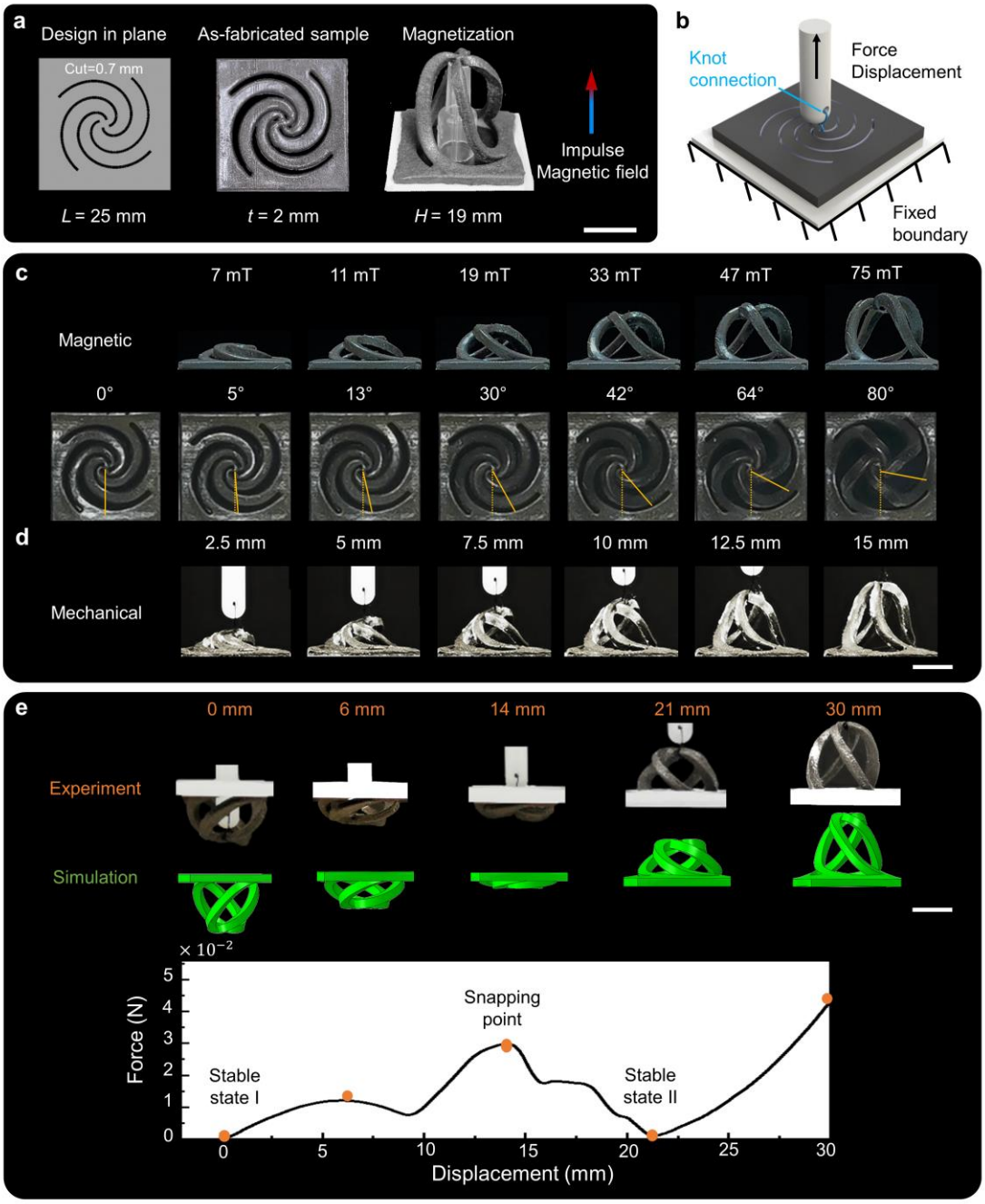

Figure S19. Manufacturing and shape morphing by mechanical force and magnetic field of the planar structure with helical cuts. a) Schematic design, as-fabricated structure, and magnetization configuration for 2D planar structure. b) Experimental setup for mechanical characterization of the structure. A plastic rod mounted to the upper clamp of a uniaxial tensile tester is connected to the center of the helical structure by wires without constraining the rotation degree of freedom. The sample is attached to a fixture on the lower clamp of a uniaxial tensile tester. c) Snapshots showing the height and rotation angle of the helical structure under different magnetic fields. d)

Snapshots of the planar helical structure at different levitations by applying a tension force at the center. e) Experimental results of the force-displacement curve, experimental and FEA simulation snapshots of the reshaped bistable 3D kirigami with helical design in tensile tests. Scale bars for all images, 10 mm.

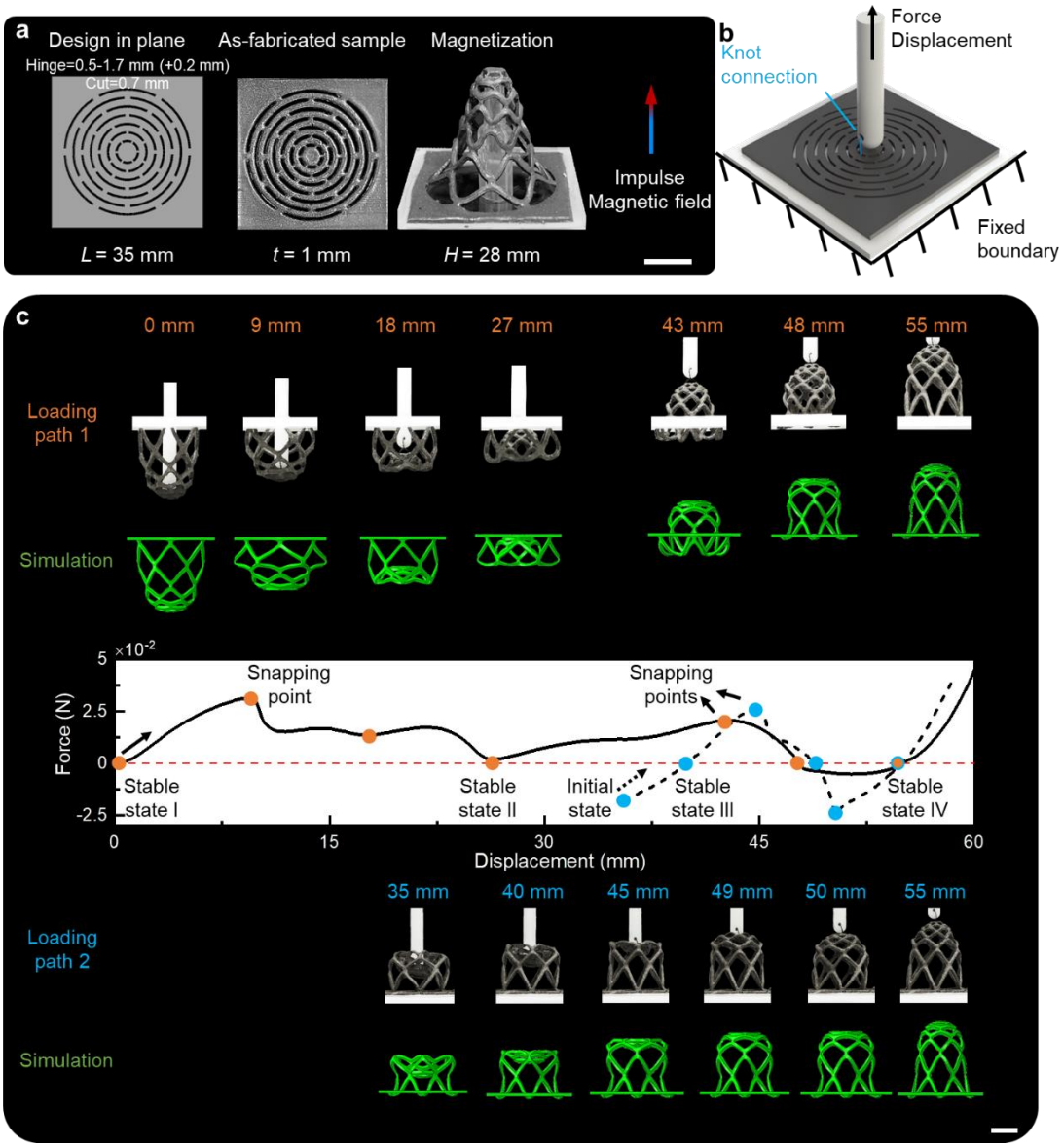

Figure S20. Fabrication and mechanical characterizations of kirigami structure. a) Schematic design, as-fabricated structure, and magnetization configuration of the planar kirigami structure with concentric arc cuts. b) Experimental setup for mechanical characterization of the planar kirigami structure. c) Experimental results of force-displacement curves by two loading paths, experimental and FEA simulation snapshots of stable states and snapping points for the reshaped 3D kirigami. Scale bars for all images, 10 mm.

Figure S21. 2D-to-3D and 3D-to-3D structural reconfigurations of MDP. Scale bar: 5 mm.

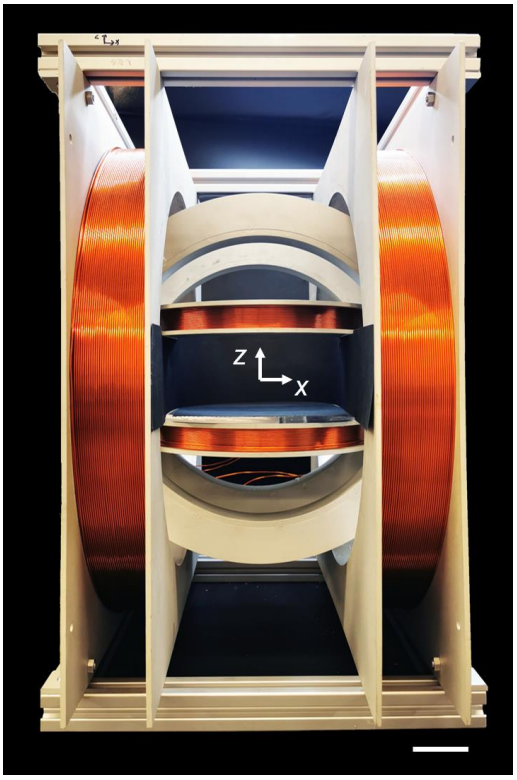

Figure S22. 3D Helmholtz coils for magnetic actuation. Scale bar: 5 cm.

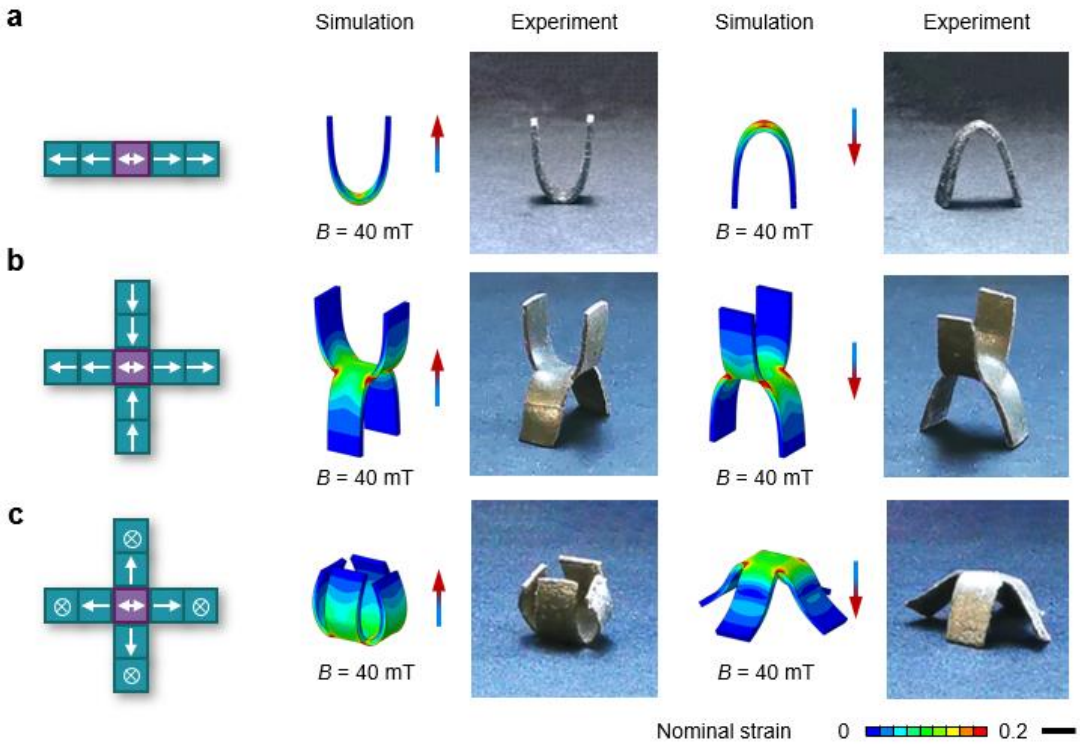

Figure S23. Finite-element analysis of the structures of the strip structure (a), cross structure (b), and cross structure with reprogrammed magnetization (c). Scale bar, 6 mm.

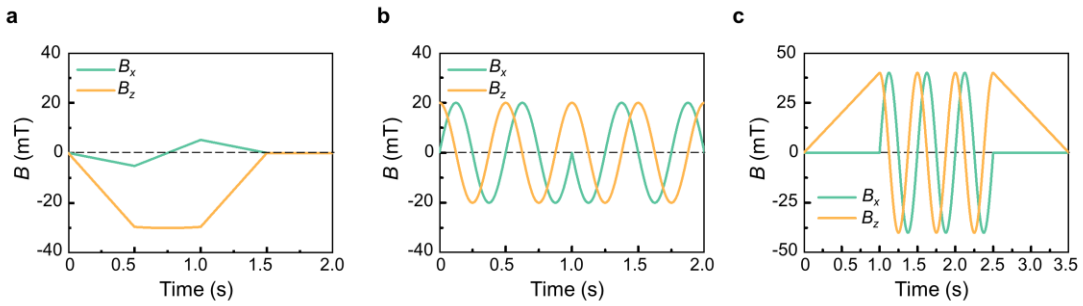

Figure S24. Magnetic profiles for the dynamic motions of the structures of strip assembly (a), cross assembly (b), and cross assembly with reprogrammed magnetization (c) in **Figure 6g**, **j**, and **l**.

Video Captions

Video S1: Magnetic-assisted assembling for seamless welding

A long strip is assembled by self-aligning of three magnetic dynamic polymer modules via dipole-dipole attraction. The assembly is welded using IR light. The welded sample is stretched to high strain without breaking.

Video S2: Magnetic-assisted modular assembling

Two square modules (single directional magnetization module and bidirectional magnetization module) are assembled to get five double-unit combination logics via dipole attraction. The modules are further assembled into various 2D planar structures with patterned magnetization followed by welding. The welded assembly including a strip, 'Z' shape, 'H' shape and square annulus shape, show out of plane shape morphing under magnetic fields, which is captured by finite element modeling.

Video S3: In-situ reprogramming of magnetization

The silicone rubber encapsulated MDP array with alternating opposite magnetization orientation in each column generates 'W' shape. The array is placed at the center of a Halbach array magnet. The array is covered by an aluminum foil photomask and exposed to IR light. With the increasing of temperature at the exposed regions, NdFeB particles are realigned and formed a chain-like structure. The magnetization of device is reprogrammed with the pixelated magnetization pointing to four centers inwards, leading to form 3D structure.

Video S4: Magnetic-assisted structural reconfiguration of kirigami with helical cuts

The planar kirigami structure with helical cuts shows fast and reversible actuation under an out-of-plane magnetic field. The planar structure is reshaped to a stress-free configuration by simultaneously applying a magnetic field using a magnet from the bottom and IR light exposure from the top. The reshaped helical architecture shows two stable states under both mechanical and magnetic actuations.

Video S5: Mechanical characterization of helical design before and after reshaping

The planar kirigami structure with helical cuts shows monostable behavior from the force-displacement curve. The reshaped 3D helical architecture shows two stable states

(minimum energy state) and a snapping point (maximum energy state) on the force-displacement curve.

Video S6: Magnetic-assisted structural reconfiguration of kirigami with concentric cuts

The planar kirigami structure with concentric arc cuts shows fast and reversible actuation under an out-of-plane magnetic field. The planar structure is reshaped to a stress-free configuration by simultaneously applying a magnetic field and IR light exposure. The reshaped concentric arc architecture shows four stable states under mechanical actuation and three stable states under magnetic actuation.

Video S7: Mechanical characterization of concentric arc design before and after reshaping

The planar kirigami structure shows monostable behavior from the force-displacement curve. The reshaped 3D concentric arc architecture shows four stable states and three global snapping points in two loading paths on the force-displacement curves.

Video S8: Combined functions: magnetic-driven modular assembly with reprogrammability and reconfigurability

Magnetic-driven remote navigation and assembling of the MDP modules with functionalities of MDP, including modular assembling and welding, in-situ magnetization reprogramming, and remote structural reshaping, are combined for multifunctional reconfiguration of rolling actuators.

Reference

[1] X. Kuang, G. Liu, X. Dong, D. Wang.Correlation between stress relaxation dynamics and thermochemistry for covalent adaptive networks polymers *Mater. Chem. Front.*, **2017**,1 111.

[2] D. Stauffer.Scaling theory of percolation clusters *Phys. Rep.*, **1979**,54,1.

[3] M. Rubinstein, A. N. Semenov.Thermoreversible Gelation in Solutions of Associating Polymers. 2. Linear Dynamics *Macromolecules*, **1998**,31,1386.

[4] A. N. Semenov, M. Rubinstein.Thermoreversible Gelation in Solutions of Associative Polymers. 1. Statics *Macromolecules*, **1998**,31,1373.

[5] P. J. Flory. Molecular Size Distribution in Three Dimensional Polymers. I. Gelation1 *J. Am. Chem. Soc.*, **1941**,63,3083.

[6] R. M. Erb, J. J. Martin, R. Soheilian, C. Pan, J. R. Barber.Actuating soft matter with magnetic torque *Adv. Funct. Mater.*, **2016**,26,3859.

[7] Y. Yang, Z. Chen, X. Song, Z. Zhang, J. Zhang, K. K. Shung, Q. Zhou, Y. Chen.Biomimetic Anisotropic Reinforcement Architectures by Electrically Assisted Nanocomposite 3D Printing *Adv. Mater.*, **2017**,29,1605750.

[8] https://mqitechnology.com/wp-content/uploads/2017/09/rn001-particle-size-distriution-en.pdf

[9] E. Guth, O. Gold, On the hydrodynamical theory of the viscosity of suspensions. Phys. Rev. **1938,**53, 322.